Sensors & Actuators: B. Chemical 353 (2022) 131085

Contents lists available at ScienceDirect

Sensors and Actuators: B. Chemical

journal homepage: www.elsevier.com/locate/snb

3D-printed low-cost fabrication and facile integration of flexible epidermal microfluidics platform

Lei Wei [a,b], Guoqing Fang [a], Zhongwen Kuang [a], Lin Cheng [a], Huaping Wu [c], Daoyou Guo [a], Aiping Liu [a,*]

[a] Key Laboratory of Optical Field Manipulation of Zhejiang Province, Zhejiang Sci-Tech University, PR China
[b] School of Physics and Electronics Engineering, Fuyang Normal University, Fuyang 236037, PR China
[c] Key Laboratory of Special Purpose Equipment and Advanced Processing Technology, Ministry of Education and Zhejiang Province, College of Mechanical Engineering, Zhejiang University of Technology, Hangzhou 310023, PR China

ARTICLE INFO

Keywords:
3D-printing
Malt syrup
Epidermal microfluidics
Sweat detection
pH sensor

ABSTRACT

Skin-mounted microfluidics devices have shown distinct advantages in sweat collection and analysis platform due to their multiple sweat treatment including sample collection, flow control, storage, analysis and expelling by special design in microfluidic networks. However, the fabrication of most reported wearable microfluidic devices with mechanical flexibility and elasticity mainly rely on soft-lithography technology whose implementation is limited by necessitating access to resource-intensive laboratory and costly facilities. Herein, we propose an accessible, low-cost fabrication and integration scheme, which renders flexible microfluidic architecture capable of performing reliable sweat collection and sensing. We utilize low-cost 3D-printing technology to rapidly yield positive mold of facile printable material (malt syrup) for personalized customization of microfluidic channels. An ingenious approach is also proposed to encapsulate microfluidic channel layer and integrate pH sweat sensor into the microfluidic device for dependable sweat collection and pH analysis. The proposed fabrication strategy of flexible and stretchable epidermal microfluidic sensor represents a low cost, reachable alternative to recently prevailing soft-lithography method, and hence significantly reduces the threshold of microfluidic development and manufacture.

1. Introduction

Emerging wearable bioanalytical devices provide a convenient manner and insightful perspective for monitoring and diagnostics of human health and fitness by accessing to biofluids and quantifying the level of biomarkers simultaneously [1–3]. Sweat is a feasible and ideal biofluid for monitoring the individual physiological status and assessing human health and fitness as it can be accessed noninvasively on surface of the skin and contains diverse biomarker from metabolites, amino acids, electrolytes to metal ions, proteins, and hormones [4–8]. Much researches indicate that the level of biomarker in sweat can reflect the health of the body [9–16]. Compared to patch- [17,18], tattoo- [19–21], and bandage- [9,11,22] wearable sweat analysis platform, epidermal microfluidic device can not only collect and analyze sweat, but also render controllable sweat flow and avert the mixture of has-been-tested sweat and to-be-tested sweat, which makes it an attractive sweat analysis platform [23–27]. The majority of reported epidermal microfluidic device based on polydimethylsiloxane (PDMS) is fabricated by soft-lithography method, where mold fabrication requires UV lithography machine in cleanroom by multi-step and time-consuming operations and every mold structure is immobilized by the design of each corresponding mask plate. These raise the threshold of microfluidic manufacturing and related technology research.

The Fused Deposition Modeling (FDM) 3D-printing is a potential low-cost fabrication technique for elastomer-based microfluidic devices [28–31]. Thermoplastics which include acrylonitrile butadiene styrene (ABS), polylactice acid (PLA), high-impact polystyrene (HIPS), nylon, poly(lactic-co-glycolic acid) (PLGA), poly(vinyl alcohol) (PVA), and high-density polyethylene (HDPE) are commonly used as 3D printing materials in the FDM technology. Most thermoplastics usually need about 200 °C to be molten before printing operation [32–39] (Table S1). A certain amount of ultra-fine particles and volatile organic compounds are released from these thermoplastic materials during 3D printing processes [40,41], which will be adverse for human health. This puts

* Corresponding author.
E-mail address: liuap@zstu.edu.cn (A. Liu).

https://doi.org/10.1016/j.snb.2021.131085
Received 23 July 2021; Received in revised form 22 October 2021; Accepted 8 November 2021
Available online 25 November 2021

forward more stringent requirements for printing equipment on temperature control, thermal insulation components, and ventilation and filtration modules. By comparison, sugar-based printing materials are environmentally friendly and have relatively lower melting temperature [42–45]. Thereinto, malt-syrup is a common sweetener with characteristics of high viscosity and semi-solid at normal temperature (left of Fig. 1a), and can become facile flowability without high heating temperature (about 80 °C). Therefore, it can be used to produce sugar painting, which is a traditional folk handicraft in China, and is created by pouring the heated malt syrup onto flattened plates manually by skilled painter. The sugar painting is vivid even if the size of its sugar filaments are not uniform (right of Fig. 1a). Inspired by this process, we print the filaments of malt syrup with precisely designed dimensions to prepare positive template for the fabrication of microfluidic channel via 3D-printing technology (Fig. 1b). The significantly low printing temperature (about 80 °C) can not only prevent oxidation or decomposition of the printing material during the heating process, but also reduce the difficulties of temperature control and thermal insulation of the 3D-printing device. In order to construct the skin-mounted microfluidics device for sweat collection and pH analysis, we propose a two-step operation for microchannel encapsulation and sensor integration via a thin uncured PDMS membrane (obtained by high-speed spin coating) as PDMS-based intermediate adhesive (PIA) with the assistance of double-sided tape (Fig. 1c-d). This two-step integration method is environmentally friendly, convenient and low-cost, without high temperature, corona discharge, surface treatment reagent or plasma treatments as used in traditional bonding methods [46–56] (Table S2). In vitro and skin-mounted experiment of microfluidic sweat sensor demonstrates the validity of our low-cost fabrication and scheme capable of reliably harvesting and analyzing sweat.

2. Material and methods

2.1. Fabrication and encapsulation of flexible microfluidic channels

A Masking tape (Youbisheng Adhesive tape, Hangzhou Co. LTD, China) was first adhered to a cleaned glass slide and cut into arcuate shape by laser cutter (ultraviolet laser marking machine-3 W, Shenzhen Chaoyue laser Intelligent Equipment Co., Ltd., China; Fig. 2a). Malt syrup (Qichun Tianli Bioengineering Co., Ltd, China) was used to print a set of sugar filaments on the glass slide by using the 3D-printing technology with the heating temperature of extruder in 80 °C, printing velocity in 5.8 mm s^{-1}, and printing distance in 400 μm. It should make sure that printing path passed through the arcuate tape (Fig. 2b). After printing filaments, the arcuate tape was peeled off to remove the filaments on the tape such that the remaining filaments reserved the structure with three endpoints which would respectively align with three inlet holes (Fig. 2c). Then, we hardened the filaments by baking them in an oven at 50 °C for 30 min to obtain the final positive mold. PDMS (mixing ratio of base to curing agent: 10:1 by weight) was poured onto the positive mold, followed by curing it in an oven at 60 °C for 4 h, and peeling off it from the glass slide to obtain microchannel layer with a thickness of 700 μm (Fig. 2d-f). By controlling the printing velocities of malt syrup (16.7 mm s^{-1}, 12.5 mm s^{-1}, 8.3 mm s^{-1}, 5.8 mm s^{-1}, 3.3 mm s^{-1}, and 1.7 mm s^{-1}, respectively), and the printing distances (0.1 mm, 0.2 mm, 0.3 mm, 0.4 mm, and 0.5 mm, respectively), sugar filaments and PDMS microchannels with different dimensions were obtained.

After that, a drop of uncrosslinked PDMS (mixing ratio of base to curing agent: 10:1 by weight) was dropped on a PDMS cover (250 μm), followed by spin-coating the uncrosslinked PDMS at 8000 r/min for 50 s to obtain a thin uncrosslinked PDMS membrane (about 2 μm in thickness), which was served as PIA to encapsulate microchannel layer by bonding microchannel layer and PDMS cover (Fig. 2g). Three inlet holes were drilled in PDMS cover by a punching pin with diameter of 2.5 mm. After covering the microchannel with the PDMS cover, the device was put into an oven with 60 °C for 2 h to cure the PIA and obtain the encapsulated microchannels.

2.2. Fabrication and integration of pH sensor in the microfluidic devices

The pH sensor was a two-electrode system. First, a cleaned polyethylene terephthalate (PET) narrow strip (12 μm in thickness, 8 mm in width) was covered by an electrode mask, and two 30-nm Ti/50-nm Au electrodes with 0.8 mm width and 1 mm distance were deposited on the PET surface by magnetron sputtering. Then one of the Ti/Au electrodes was activated by cyclic voltammetry (CV) from − 0.2–1.6 V versus a commercial Ag/AgCl reference electrode for 10 circles at a scan rate of 0.1 V/s in the aqueous solution containing 0.5 M sulfuric. After that, a polyaniline (PANI, purchased from Aladdin Industrial Corporation, China) film was electrochemically polymerized on the activated Ti/Au electrode via CV from − 0.2–1.0 V versus Ag/AgCl electrode at a scan

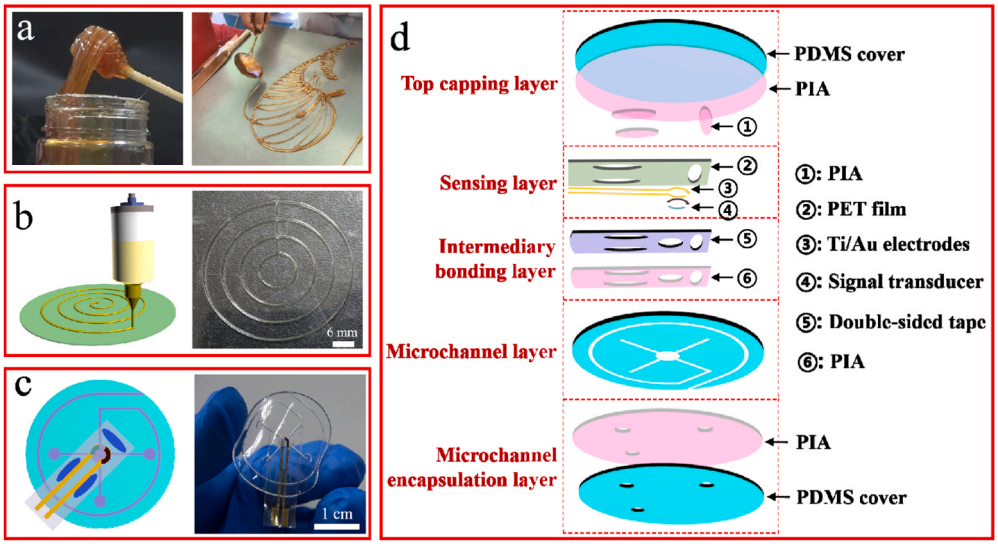

Fig. 1. The fabrication and integration scheme of 3D-printing flexible microfluidic platform for sweat pH sensing. (a) Malt syrup with high viscosity in room temperature (left), and sugar painting made of malt syrup (right). (b) Diagram of 3D printing sugar filament (left), and the printed sugar filament (right). (c) The assembled microfluidic sweat sensor. (d) Exploded view of microfluidic sweat sensor.

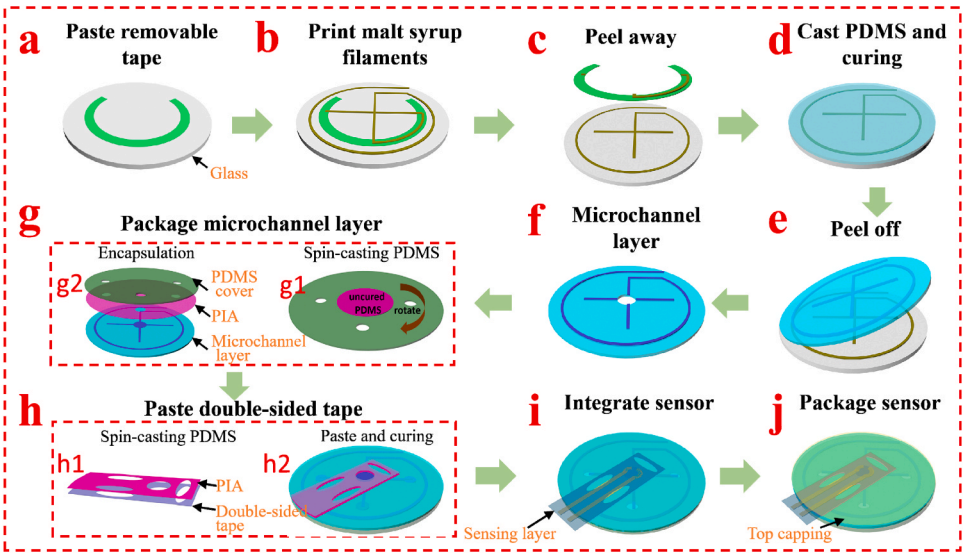

Fig. 2. Fabrication procedure of the microfluidic sweat sensor which can be divided into three main steps: (a)-(c) preparation of positive template, (d)-(g) preparation and encapsulation of microfluidic channel, (h)-(j) integration of sensor into microfluidic channel. The details are as follows. (a) Arc shaped removable tape was fabricated on a glass slide by laser cutting. (b) Filaments were printed on the glass slide and a section of arc shaped filament was printed on the arc shaped tape. (c) Filaments on the tape was removed by peeling off the tape, thus the microchannel network with four endpoints was obtained. Three endpoints were used as inlets of sweat, and the fourth one was used as an outlet. (d) The PDMS was casted on positive mold and cured. (e) The cured PDMS was peeled off to (f) obtain microchannel layer. (g) Convenient encapsulation of microchannel layer was achieved by the following two steps: (g1) spinning coating uncrosslinked PDMS on a PDMS cover to form a thin uncrosslinked PDMS film served as PIA, then punching three holes as inlets of the microfluidic chip, (g2) encapsulating the microchannel layer with the PIA coated PDMS cover. After PIA was cured, the encapsulation of microchannel layer was finished. Integrating sensor into microfluidic chip by the follow three steps: (h) pasting double-sided tape on microchannel layer with the assistance of PIA, (i) pasting sensing layer on double-sided tape, (j) encapsulating the sensing layer with a PDMS-based top capping with assistance of PIA.

rate of 0.1 V/s in the solution containing 0.1 M aniline and 1 M HCl, obtaining the Ti/Au/PANI working electrode on the PET substrate. For the reference electrode preparation, the other Ti/Au electrode was screen-printed Ag/AgCl ink (Shanghai Julong Electronic Technology Co., Ltd, China) and dried under 4 °C without light, followed by the modification with a mixture solution including 79.1 mg Polyvinyl butyral (PVB, purchased from Aladdin Industrial Corporation, China), 50 mg NaCl, and 2 mg poly(ethylene glycol)-block-poly(propylene glycol)- block-poly(ethylene glycol) (F127, purchased from Aladdin Industrial Corporation, China) in 1 mL methanol.

In order to integrate the pH sensor in the microfluidic device, a stripe of double-sided tape (9495LE 300LSE, 3 M, USA) with three oval holes and a circular hole with 4-mm diameter was pasted on the microchannel layer with the assistance of PIA which was prepared by spin-coating at 8000 r/min for 50 s (Fig. 2h) and cured at 60 °C for 2 h. Then the PET stripe with pH sensor was adhered to the double-sided tape and the sensor layer with a PDMS-based top capping was encapsulated with the assistance of PIA (Fig. 2i-j). In all the adhesion operations, the alignment of holes with sensor was critical.

2.3. Characterization of the microchannel samples and pH sensors

The sections of microchannels with different dimensions were characterized by scanning electron microscopy (SEM, Hitachi S4800, Japan). The bonding strength of different interfaces in the microfluidic device with integrated senor were characterized via T-type peeling test on Digital Variable-Speed Motorized Test Stands (MX-U350, Jiangsu Moxin Industrial System Co., Ltd, China) with test sample width of 13 mm and peeling rate of 10 mm min^{-1}. The fabrication methods of the test interfaces were as follow. Bond two cured PDMS strips with the aid of PIA to form Interface 1. Bond double-sided tape onto PDMS strip with the aid of PIA to form Interface 2. Stick PET film onto double-sided tape to form Interface 3. Stick PDMS strip onto double sided tape directly to form Interface 0, which was served as a control group.

The properties of the individual pH sensor, including pH sensing behavior, repeatability, long-term stability, temperature dependency, and selectivity were tested in the Britton-Robison buffer solutions with different pH levels (4.1, 5.0, 6.0, 7.0, 7.7, 8.8), which were prepared by adding 0.2 M NaOH solution with varying volumes into 0.04 M mixed acid of phosphoric acid, boric acid and acetic acid of 100 mL. The pH sensor readout was recorded by electrochemical workstation (CHI 660E, Shanghai Chenhua Instrument Co., Ltd, China) in each test. The stability of the pH sensor was demonstrated by potential drift test in one hour in the solution with pH levels of 4.1, 7.0, 8.8. The selectivity test of pH sensor was carried out by subsequently adding possible interfering electrolytes (1 mM Ca^{2+}, 1 mM Mg^{2+}, 5 mM K^{+}, 20 mM Na^{+},) and Britton-Robison buffer solution of pH 7.0 into a Britton-Robison buffer solution of pH 6.0. The temperature dependency of the sensor was evaluated from 15° to 30°C with the interval of 5 °C in Britton-Robison buffer solution with the pH level of 4.1, 7.0, and 8.8, respectively.

2.4. In-vitro and on-body electrochemical characterization of microfluidic device with integrated sensor

The in-vitro electrochemical characterization of microfluidic device with integrated pH sensor was performed by flow injection analysis. A syringe pump (LSP01–3A, Baoding Lange constant flow pump Co., Ltd, China) was used to pump the test solution into the microfluidic device from the outlet of microfluidic device where one end of an amputated syringe needle was inserted into the microchannel and the other end was inserted into a flexible tube. The flexible tube was connected to the syringe. The test solution flowed out of device from one of the inlets, while the other two inlets was sealed by adhesive tape (Fig. S1). The repeatability of the microfluidic device with integrated pH sensor in flow injection test was carried out at a flow rate of 10 μL/min with varying pH levels (4.1, 5.0, 6.1, and 7.0). The outputs of the sensor were recorded by electrochemical workstation. The effect of flow rate of test solution on the output behavior of the sensor was investigated with three different injection flow rates (10, 17, and 33 μL·min^{-1}). The response of the device under various deformations, including bending, stretching, and twisting was also recorded when the test solution was injected into the microfluidic device to fill the sensing chamber.

The on-body sweat test analysis was implemented on two healthy young volunteers. Each volunteer had been given full, informed consent before participating in the test. The microfluidic device was adhered to volunteers' forehead by double-sided tape (9495LE 300LSE, 3 M, USA) after the skin at adhesion site was cleaned with alcohol to dispel ash and grease. In sweat collection test, sweat was induced by continuous

outdoor running for one of volunteers and being exposed to hot indoor (33 °C) for the other volunteer. The sweat collection process was tracked and recorded by a camera. In on-body sweat pH test, sweat was induced by being exposed to hot indoor (33 °C), and during the process a volume of warm water was intake to maintain water balance in the body, and the outputs of the sensor were recorded by the electrochemical workstation.

3. Results and discussion

3.1. Quantitative size analysis of microfluidic channel obtained from sugar filament mold fabricated by precision-controlled 3D-printing technology

The 3D-printing system consists of five subsystems, namely 3D motion platform, sugar extruder, temperature control system, pneumatic control system and computer (Fig. S2). Malt syrup in extruder is squeezed out of printing nozzle (510 μm in internal diameter) by pressured gas (70 psi), meanwhile printing nozzle driven by 3D motion platform moves according to the predefined printing path in printing control software. Thus the squeezed sugar filaments are written on glass slide to create patterned structures (Fig. 1b and Fig. S3). However, the malt syrup fails to squeeze out of printing nozzle at normal temperature because of its high viscosity. Therefore, the malt syrup needs to be heated to 80 °C by temperature control system to enhance its liquidity. After the printed filament on glass slide are dried at 50 °C for 30 min to evaporate water and harden the filament, we can obtain positive mold. The hardened mold can keep performance stable for at least 2 months in an oven even the oven temperature rises to 70 °C. Then PDMS is casted on glass slide to cover the positive mold then cured at 60 °C for 4 h, and the microchannel is obtained after peeling off the cured PDMS from glass slide. The positive molds can still remain solid in the general ambient humidity (relative humidity 70–80% at 25 °C) at least 5 days and can be used repeatedly.

In order to precisely design and control the sugar filament dimension, we built a 3D-printing model as shown in Fig. 3a. Flux of the sugar squeezed out of the nozzle (denoted as Q) and translational speed of the nozzle (denoted as v) determine the filament dimension, and Q can be expressed by

$$Q = Sv, \tag{1}$$

where S is section area of filament. Ignoring the effect of gravity, the shape of filament section is circular. Thus, the nominal radius of filaments is

$$r_0 = \sqrt{\frac{Q}{\pi v}}. \tag{2}$$

The impact factors of Q include air pressure, temperature of malt syrup and internal diameter of nozzle, whose values are set to be 70 psi, 80 °C, and 510 μm, respectively. Thus, Q is constant, and the dimension of filament is inversely proportional to square root of v in case of ignoring gravity. In practice, we find that the distance between bottom surface of nozzle and printing plane (denoted as H, as illustrated in Fig. 3a) affects the printing result. Specifically, the nozzle may fail to write an intact filament in case of abnormal large H, or compresses filament to flat structure in case of abnormal small H. To further study the impact of control parameters on filament dimension, we prepared a set of microchannels under different v and H and obtained the section images of the microchannels. The SEM images show that the sections of microchannels are usually non-holonomic circle (Fig. S4) due to the combined effect of surface tension, gravity, and compression of nozzle. The surface tension renders filament ability to spontaneously form cylindrical shape during the cooling process [44,45], while gravity and the compression of nozzle impel the section to non-holonomic circle. The compression even leads to serious deformation of sugar filament when H is much small (such as H=100 μm, Fig. S4). The microchannel dimension decreases with the increase of v for a given H (Fig. 3b and Fig. S5a). By analyzing the change of average microchannel widths and heights with different H as illustrated in Fig. 3c, we find that H has

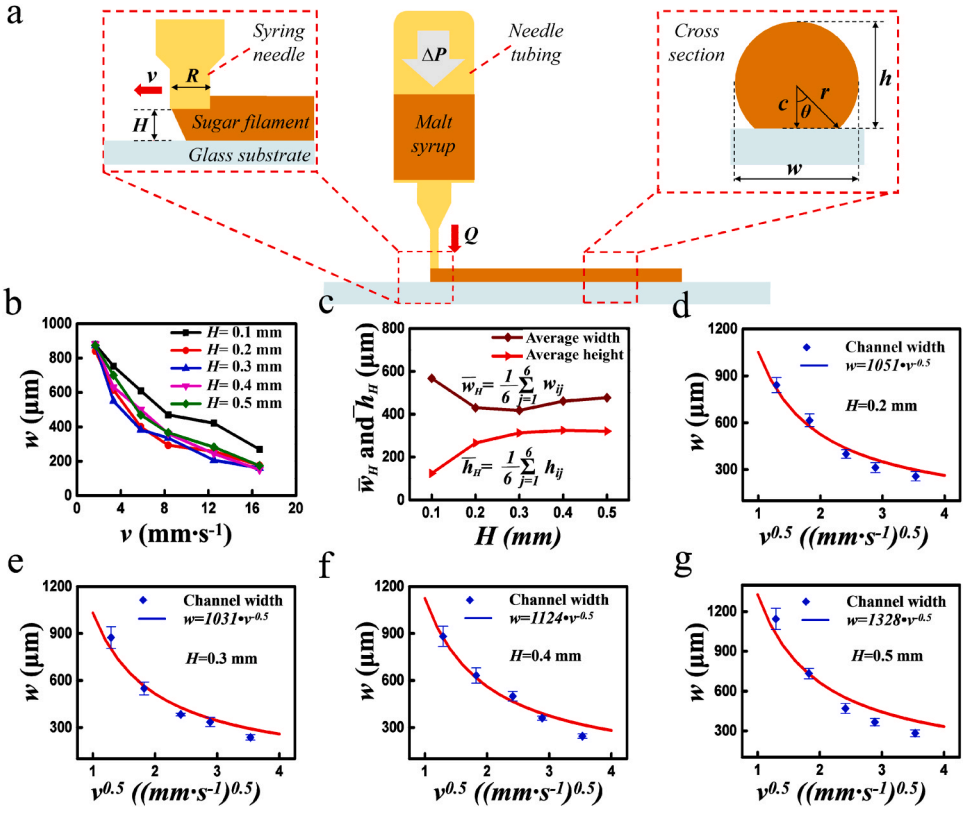

Fig. 3. (a) 3D-printing model of microchannel. (b) The relation of microchannel width and v in case of different H. (c) The change of average width and average height with H. Here $\bar{h}_H$ is the average height of microchannels under a certain H, and $\bar{w}_H$ is the average width of microchannels under a certain H, and h_{ij} is the height of microchannel in this case of H=H_i and v=v_j, and w_{ij} is the width of microchannel in this case of H=H_i and v=v_j. (d)-(g) The relationship between width of microchannel and the square root of v in case of different H. Discrete points are the average of experimental data (N = 3), with the error bars representing the standard diviation, and the smooth curves are the fitting results of inversely proportional function.

inconspicuous effect on microchannel dimension excluding abnormal small H. Similarly, Fig. S5b clearly reveals that v is the major factor to regulate filament and microchannel dimensions.

The filament may go through stretching, self-heaping, or compression during the printing process. If the traveling distance of nozzle is larger than natural extrusion length of filament in unit time, the filament will be stretched, otherwise, the filament will be self-heaped. Besides, if the diameter of the filament is larger than H, the filament will be compressed by bottom surface of nozzle. The deformation of the newly extruded filament can be divided into the following three cases. Case 1: $2r_0<H$, namely, the filament will not be compressed by the bottom surface of nozzle. In this case, filament section usually inclines to be complete circle due to its surface tension and less effect of gravity. Case 2: $H< 2r_0<R$ (R is the nozzle diameter, as illustrated in Fig. 3a), which means that the filament is still stretched but nominal diameter ($2r_0$) of filament is greater than H. Thus the filament will be compressed by the bottom surface of nozzle, and its section will be non-holonomic circle. Case 3: $2r_0>R$, namely, the traveling distance of nozzle is less than natural extrusion length of filament in unit time. The new extruded filament will heap against the old one. In this case, the compression of nozzle and the effect of gravity impel the filament to be more non-holonomic circle. The three cases can be realized by regulating the v according to Eq. (2). In order to quantitatively analyze the relationship between microchannel dimension and v, we supposed that the section of microchannel is a part of a circle according to Fig. S4, and built the section model of microchannel (Fig. 3a), where r is the radius of microchannel, c is distance between the center of microchannel and printing plane, and θ is an inner angle of right triangle ($0 < \theta < \frac{\pi}{2}$). The section area of microchannel can be written as

$$S = \left[\left(\pi - \arccos\frac{c}{r}\right) + \frac{c}{r}\sqrt{1-\left(\frac{c}{r}\right)^2}\right]r^2 = (\pi - \theta + 0.5\sin 2\theta)r^2 \quad (3)$$

Let

$$\lambda = \pi - \theta + 0.5\sin 2\theta, \quad (4)$$

we get

$$r = \left(\frac{Q}{\lambda}\right)^{0.5} v^{-0.5}. \quad (5)$$

As illustrated in Eq. (5), there is no strict inversely-proportional relationship between r and the square root of v because λ is variable. Considering the application of epidermal microfluidics, where the microchannel width is commonly designed between 200 μm and 800 μm, the v should vary approximately from 3 to 12 mm s^{-1} according to experimental experience. In this case we could obtain that $\lambda^{-0.5}$ varies in a small range of 0.57–0.73 (more details in Table S3 and related analysis). Therefore, the microchannel dimension is approximately inversely proportional to the square root of v in fabrication process of epidermal microfluidics. To demonstrate the inverse-proportion relationship, we used the experimental data of w_{ij} ($j = 1, 2, \ldots,5$, corresponding to v=1.67, 3.33, 5.83, 8.33, and 12.50 mm s^{-1}) to fit and obtain the inverse-proportion coefficient at the situation of each H_i (H_i =200 μm, 300 μm, 400 μm, and 500 μm), as illustrated in Fig. 3d–g. The fitting results show that the width of microchannel w and the square root of v can fit inversely proportional function well. This relationship can provide us guidance for the regulation of microchannel dimension.

3.2. Interface characteristics of epidermal microfluidic device with integrated sweat pH sensor

Fig. 1d illustrates the exploded view of the epidermal microfluidic device which consists of microchannel layer, microchannel encapsulation layer, sensing layer, intermediary bonding layer (used to integrate sensing layer into the microfluidic chip), and top capping layer. When the device is bonded to the skin by a double-sided adhesive tape, sweat excreted from eccrine glands first accesses to the inlets and quickly fills them, then travels through microchannels into circular detection chamber in which pH sensor is integrated, and eventually flows out of detection chamber through microchannel upon filling the chamber (Fig. 1c). This process ensures the renewal of sweat in detection chamber.

Conventional lithographical method for the fabrication of PDMS-based microfluidic devices depends on resource-intensive cleanroom procedures and fixed-design mask to create positive mold, and requires plasma etcher to encapsulate microfluidic devices. Here the fabrication and integration scheme based on the proposed 3D-printing technology is low-cost and flexible. The scheme consists of three main steps, namely printing of sugar filament mold, preparation and encapsulation of microfluidic channels, and pH sensor integration and system encapsulation (Fig. 4a–c, more details in Fig. 2). For encapsulation of microfluidic channels, PIA prepared by spin-coating uncrosslinked PDMS (8000r/min, 50 s) on a PDMS cover to form a thin membrane to bond microchannel layer and PDMS cover when PIA curing (Fig. 4e). The satisfactory adhesion between microchannel layer and PDMS cover is validated by the apparent rough traces after peeling off the bonded interface (Fig. S6). The robustness of this encapsulation method was proved by tensile test of the encapsulated microchannel with 30% tensile for 100 cycles. The well-preserved microchannels after tensile test (Fig. S7) demonstrate the reliability of encapsulation scheme and provide an alternative to routine use of plasma treatment in microfluidic channel encapsulation.

When a pH sensor was integrated into sweat collection reservoir to form a detection chamber, a double-sided tape was served as an intermediary bonding layer to combine the microchannel layer and sensing layer, therefore double-sided tape was bonded onto the upper surface of microchannel layer and PIA was used to enhance the adhesion strength (Fig. 4e). Three different interfaces were formed in the process of microchannel encapsulation and sensor integration, as illustrated in Fig. 4e. The excellent adhesion strength of these interfaces was verified by a T-type peeling test. As shown in Fig. 4f, the adhesion strength of the bonding interface treated by PIA (Interface 1 and Interface 2) is significantly bigger than untreated one (Interface 0), which ensures reliable integration of the whole microfluidic device. The PDMS in elliptic holes also serves as PIA to clamp and fix the sensing layer after the PDMS is cured (Fig. 2h-j). When the microfluidic device with integrated sensor is stretched, the whole device becomes oval, while the detection chamber remained circular due to the non-stretchability of PET substrate (Fig. 4d), which implies the excellent adhesion strength of multiple interfaces.

3.3. pH detection via epidermal microfluidic platform with integrated sweat pH sensor

Analysis of sweat pH level is a significant matter as it can be used to characterize metabolic alkalosis [57], or to correct the pH-dependent deviation of sweat sensor such as enzyme-based glucose sensor [13] or sweat ionized calcium sensor [11]. The pH detection is achieved via the deprotonation and protonation process at the surface of PANI film, which leads to the change of Open Circuit Potential (OCP) versus reference electrode [11]. Fig. 5a illustrates the dynamic OCP responses of pH sensor to consecutive variation of pH level alternately from low to high and then from high to low. The rapid and consistent output of the pH sensor indicates good repeatability of the response in physiological relevant range of sweat pH. The corresponding linear calibration curve in pH range from 4 to 9 shows great linearity with a high resolution of 60.8 mV pH^{-1} (R-squared value of 0.999) and a near-Nernst behavior [2,58] (Fig. 5b). The stability test over an hour under three constant pH levels shows small potential drifts (ΔV) (Fig. 5c). Additionally, the pH sensor displays excellent selectivity to pH level of solution when exposed

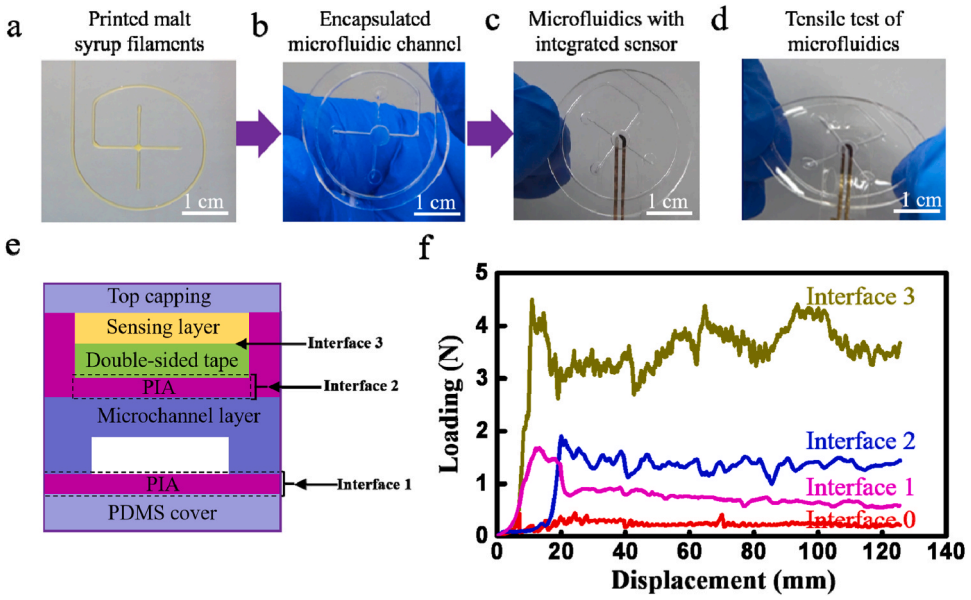

Fig. 4. Illustration of microfluidic device fabrication and integration scheme. The scheme consists of three main steps, namely (a) printing positive mold of syrup filaments, (b) encapsulation of microfluidic channel, and (c) integration of senor into the microfluidic device. (d) Tension test of microfluidic device with integrated sensor. (e) The scheme of microchannel encapsulation and sensor integration. (f) Adhesion strength test of different interfaces.

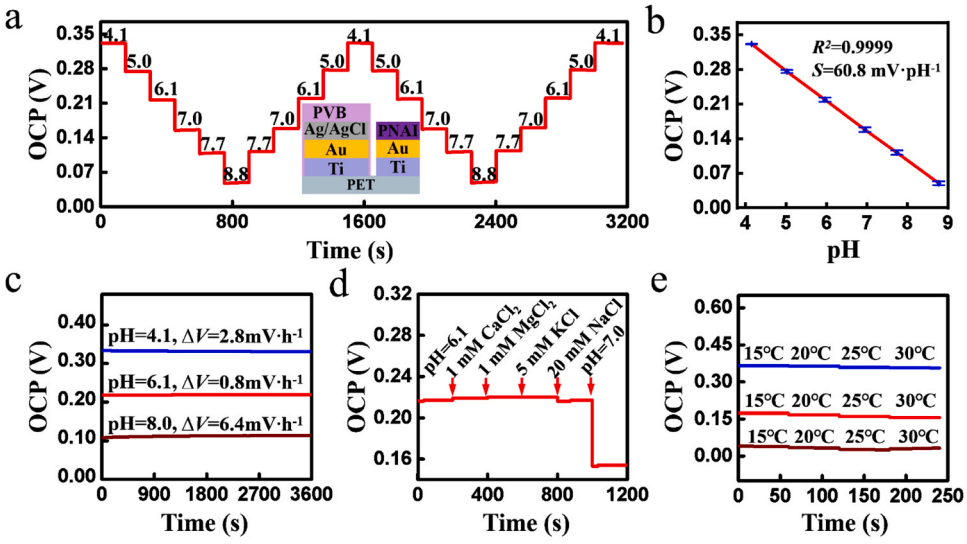

Fig. 5. OCP characterization of pH sensor measured versus Ag/AgCl reference electrode. (a) The OCP response of the sensor in the solution with different pH levels (inset: compositions of a reference electrode and pH sensing electrode). (b) The calibration curve of pH sensor (N = 4), with the error bars representing the standard diviation. (c) Stability of the sensor during one-hour continuous measurement. (d) The selectivity test of the sensor to potential interfering substances in human sweat. (e) Temperature stability of the sensor tested in pH level of 4.1, 7.0, 8.8, respectively.

to the possible interfering electrolytes in physiological relevant ranges (1 mM Ca^{2+}, 1 mM Mg^{2+}, 5 mM K^{+}, 20 mM Na^{+}). The output of the sensor slightly changes when the sensor is exposed to the solution containing 20 mM Na^{+} (Fig. 5d). Besides, the output of the sensor is barely affected by temperature (Fig. 5e and Fig. S8a), and can keep stability in bending state of 45 degrees (Fig. S8b). Potential stability of reference electrode is also as important as the accuracy of working electrode for accurate measurement. Our testing indicates that the PVB-coated Ag/AgCl reference electrode (PVB electrode) can not only greatly eliminate the distraction from external chloride ions in the solution, and remains the potential stable with changeable pH level and environment temperature, but also keep wonderful long-term stabilities (Fig. S9). These characterizations above indicate that the pH sensor is reliable for accurate analysis of sweat pH level.

The dynamic response of the pH sensor integrated in microfluidic device was also tested by injecting a set of buffer solutions with stepwise changing pH levels, and OCP of working electrode versus Ag/AgCl reference electrode was recorded by electrochemical workstation (Fig. 6a). Fig. 6b shows excellent repeatability of the pH sensor. The update time of the solution in detection chamber is affected by the injection rate (Fig. 6c), and is approximately inversely proportional to the rate (Fig. S10), which is consistent with previously reported work [16]. Under various, repetitive mechanical deformations, including bending, stretching, and twisting, the OCP of pH sensor integrated in microfluidic device will emerge noises but it can quickly recover to previous level after removing these deformations. (Fig. 6d).

In order to validate the ability of our scheme in term of on-body sweat collection and analysis, the microfluidic device without integrating sensor was adhered to skin by double-sided tape (Fig. 7a). The sweat collection experiments involved two human subjects whose sweat was induced by continuous outdoor running (subject A) or being exposed to hot indoor heated with air conditioner (subject B) while the outdoor temperature was about 30 °C. To highlight the collected sweat in microchannel, a drop of dye solution (Sudan red) was carefully added

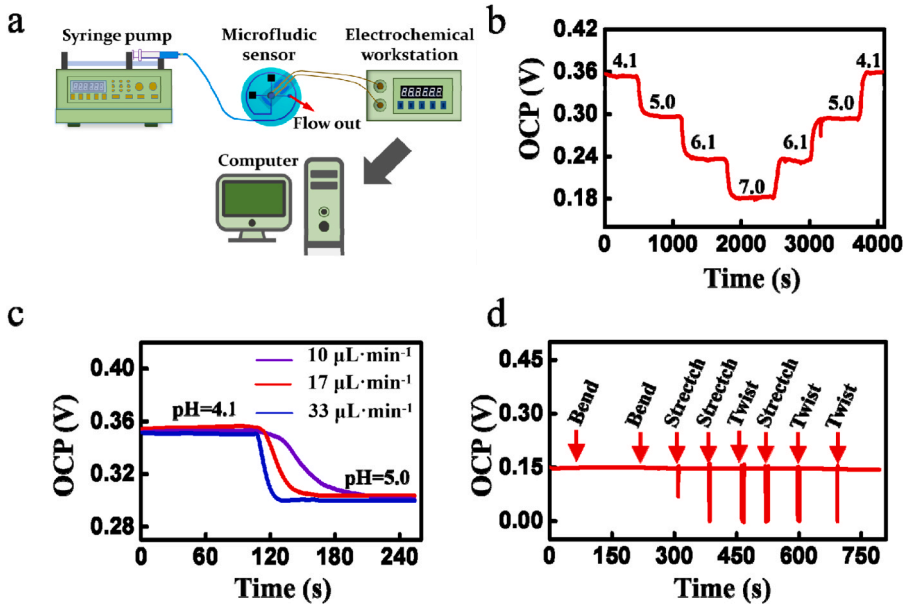

Fig. 6. Flow injection test in microfluidic device with integrated pH sensor. (a) Schematic of the flow injection test system. (b) Repeatability of the integrated sensor are tested under a pump rate of 10 μL·min^{-1}. (c) Response of pH stepwise changes at three different flow rates of 10, 17, and 33 μL·min^{-1}, respectively. (d) The responses of the integrated sensor under various, repetitive mechanical deformations.

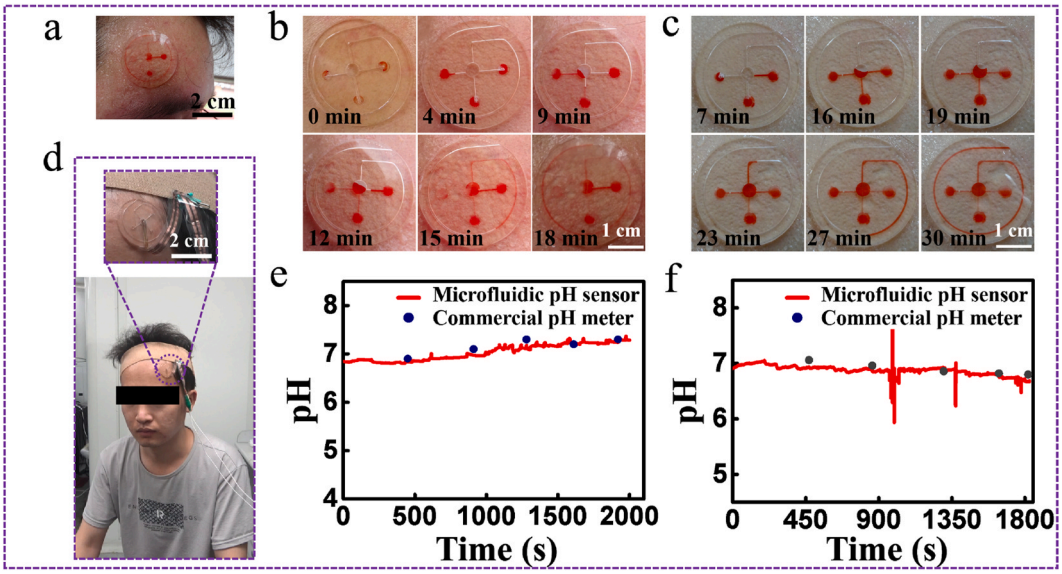

Fig. 7. On-Body sweat analysis of the integrated sensor. (a) The microfluidic chip is adhered to forehead for sweat collection. (b) Sweat collection during outdoor running or (c) sedentary state with exposured to hot environments indoor. (d) Depiction of on-body microfluidic device configuration adhered to the forehead of the subject. Real-time analysis results of sweat pH level of subject A (e) and subject B (f), and blue dots in the figures are the values of sweat pH level measured by a commercial pH meter.

to each inlet of microfluidic sensor before the sensor was mounted onto the skin, then water was evaporated in room temperature to retain only the Sudan red dye. In sweat collection trial, the sweat in the inlets dissolved the dye and turned red in color. The devices could capture adequate sweat to fill reservoir without lateral leakage during outdoor running or sedentary state exposed to hot environments. In outdoor test, the time to fill the reservoir is approximate 13 min (Fig. 7b), while in indoor test , the time is about 20 min (Fig. 7c). Then, the microfluidic device with integrated pH sensor was adhered to two subjects' forehead who were exposed to hot indoor (Fig. 7d). When sweat filled the detection chamber that can ensure consistent and stable output of pH sensor, the real-time, continuous signal output from pH sensor was acquired with electrochemical workstation. In order to verify the accuracy of sweat pH measurement, the sweat was simultaneously collected manually and analyzed by commercial pH meter (Beijing shunkeda Technology Co., Ltd, China) during the measurements. The pH acquired from the microfluidic device fits well with the results acquired from commercial pH meter at these discrete sweat sampling points (Fig. 7e and f). The results of two individuals' sweat pH analysis hint the utilization of the proposed scheme for fabrication of wearable sweat sensor.

4. Conclusion

In conclusion, we reported a low-cost, 3D-printing fabrication and integration scheme of PDMS-based epidermal microfluidic device. In this scheme, malt syrup was used as printing material to produce positive mold. We found that the printing velocity is the key influence factor of microchannel dimension, whose square root is approximately inversely proportional to microchannel dimension in the application of epidermal microfluidics fabrication. Uncrosslinked PDMS was used as an adhesive to robustly encapsulate microfluidic channel layer and to integrate sensor into the microfluidic device, which was a good alternative to traditional bonding method of plasma treatment. In-vitro and on-body measurement demonstrated that the proposed 3D-printing scheme provided a reliable, low-cost path to fabricate epidermal microfluidic sweat sensor. Future studies would focus on developing fully integrated sweat patch with flexible circuits capable of in-situ readout and wireless transmitting analyzed data to mobile devices, and to develop simultaneous multiple parameters analysis on a single 3D-printing microfluidic device.

CRediT authorship contribution statement

Lei Wei: Methodology, Software, Data curation, Writing – original draft preparation. **Guoqing Fang:** Data curation, Software, Validation. **Zhongwen Kuang**: Software, Validation. **Lin Cheng:** Formal analysis, Investigation. **Huaping Wu:** Investigation. **Daoyou Guo:** Investigation. **Aiping Liu:** Supervision.

Declaration of Competing Interest

The authors declare that they have no known competing financial interests or personal relationships that could have appeared to influence the work reported in this paper.

Acknowledgements

This work was supported by the Zhejiang Outstanding Youth Fund of China (No. LR19E020004), the Youth Top-notch Talent Project of Zhejiang Ten Thousand Plan of China (No. ZJWR0308010), the National Natural Science Foundation of China (No. 11672269 and 11972323), the Zhejiang Provincial Natural Science Foundation of China (No. LR20A020002), and the Fundamental Research Funds for the Provincial Universities of Zhejiang of China (No. RF-B2019004).

Appendix A. Supporting information

Supplementary data associated with this article can be found in the online version at doi:10.1016/j.snb.2021.131085.

References

[1] Y. Yang, W. Gao, Wearable and flexible electronics for continuous molecular monitoring, Chem. Soc. Rev. 48 (2019) 1465–1491, https://doi.org/10.1039/c7cs00730b.
[2] A. Bandodkar, W. Jeang, R. Ghaffari, J. Rogers, Wearable sensors for biochemical sweat analysis, Annu. Rev. Anal. Chem. 12 (2019) 1–22, https://doi.org/10.1146/annurev-anchem-061318-114910.
[3] F. Criscuolo, I.N. Hanitra, S. Aiassa, I. Taurino, N. Oliva, S. Carrara, G.D. Micheli, Wearable multifunctional sweat-sensing system for efficient healthcare monitoring, Sens. Actuators B: Chem. 328 (2021), 129017, https://doi.org/10.1016/j.snb.2020.129017.
[4] M. Bariya, H.Y.Y. Nyein, A. Javey, Wearable sweat sensors, Nat. Electron. 1 (2018) 160–171, https://doi.org/10.1038/s41928-018-0043-y.
[5] M. Chung, G. Fortunato, N. Radacsi, Wearable flexible sweat sensors for healthcare monitoring: a review, J. R. Soc. Interface. 159 (2019), 20190217, https://doi.org/10.1098/rsif.2019.0217.
[6] C. Legner, U. Kalwa, V. Patel, A. Chesmore, S. Pandey, Sweat sensing in the smart wearables era: towards integrative, multifunctional and body-compliant perspiration analysis, Sens. Actuators A Phys. 296 (2019) 200–221, https://doi.org/10.1016/j.sna.2019.07.020.
[7] M.C. Brothers, M. DeBrosse, C.C. Grigsby, R.R. Naik, S.M. Hussain, J. Heikenfeld, S. S. Kim, Achievements and challenges for real-time sensing of analytes in sweat within wearable platforms, Acc. Chem. Res. 52 (2019) 297–306, https://doi.org/10.1021/acs.accounts.8b00555.
[8] R. Ghaffari, J.A. Rogers, T.R. Ray, R. Recent progress, challenges, and opportunities for wearable biochemical sensors for sweat analysis, Sens. Actuators B: Chem. 332 (2021), 129447, https://doi.org/10.1016/j.snb.2021.129447.
[9] S. Emaminejad, W. Gao, E. Wu, Z.A. Davies, H.Y. Y. Nyein, S. Challa, S.P. Ryane, H. M. Fahad, K. Chen, Z. Shahpar, S. Talebi, C. Milla, A. Javey, R.W. Davis, Autonomous sweat extraction and analysis applied to cystic fibrosis and glucose monitoring using a fully integrated wearable platform, Proc. Natl. Acad. Sci. U. S. A., Early Ed. 114 (2017) 4625–463, ⟨http://doi.org/10.1073/pnas.1701740114⟩.
[10] J. Gonzalo-Ruiz, R. Mas, C. de Haro, E. Cabruja, R. Camero, M.A. Alonso-Lomillo, F.X.M. Pascual, Early determination of cystic fibrosis by electrochemical chloride quantification in sweat, Biosens. Bioelectron. 24 (2009) 1788–1791, https://doi.org/10.1016/j.bios.2008.07.051.
[11] H.Y.Y. Nyein, W. Gao, Z. Shahpar, S. Emaminejad, S. Challa, K. Chen, H.M. Fahad, L.-C. Tai, H. Ota, R.W. Davis, A. Javey, A wearable electrochemical platform for noninvasive simultaneous monitoring of Ca2+ and pH, ACS Nano 10 (2016) 7216–7224, https://doi.org/10.1021/acsnano.6b04005.
[12] Y. Chen, S. Lu, S. Zhang, Y. Li, Z. Qu, Y. Chen, B. Lu, X. Wang, X. Feng, Skin-like biosensor system via electrochemical channels for noninvasive blood glucose monitoring, Sci. Adv. 3 (2017), e1701629, https://doi.org/10.1126/sciadv.1701629.
[13] H. Lee, T.K. Choi, Y.B. Lee, H.R. Cho, R. Ghaffari, L. Wang, H.J. Choi, T.D. Chung, N. Lu, T. Hyeon, S.H. Choi, D.-H. Kim, A graphene-based electrochemical device with thermoresponsive microneedles for diabetes monitoring and therapy, Nat. Nanotechnol. 11 (2016) 566–572, https://doi.org/10.1038/NNANO.2016.38.
[14] H. Xia, H. Tang, B. Zhou, Y. Li, X. Zhang, Z. Shi, L. Deng, R. Song, L. Li, Z. Zhang, J. Zhou, Mediator-free electron-transfer on patternable hierarchical meso/macro porous bienzyme interface for highly-sensitive sweat glucose and surface electromyography monitoring, Sens. Actuators B: Chem. 312 (2020), 127962, https://doi.org/10.1016/j.snb.2020.127962.
[15] Y. Zhang, H. Guo, S.B. Kim, Y. Wu, D. Ostojich, S.H. Park, X. Wang, Z. Weng, R. Li, A.J. Bandodkar, Y. Sekine, J. Choi, S. Xu, S. Quaggin, R. Ghaffari, J.A. Rogers, Passive sweat collection and colorimetric analysis of biomarkers relevant to kidney disorders using a soft microfluidic system, Lab Chip 19 (2019) 1545–1555, https://doi.org/10.1039/c9lc00103d.
[16] Y. Yang, Y. Song, X. Bo, J. Min, O.S. Pak, L. Zhu, M. Wang, J. Tu, A. Kogan, H. Zhang, T.K. Hsiai, Z. Li, W. Gao, A laser-engraved wearable sensor for sensitive detection of uric acid and tyrosine in sweat, Nat. Biotechnol. 38 (2019) 217–226, https://doi.org/10.1038/s41587-019-0321-x.
[17] H. Lee, C. Song, Y.S. Hong, M.S. Kim, H.R. Cho, T. Kang, K. Shin, S.H. Choi, T. Hyeon, D.-H. Kim, Wearable/disposable sweat-based glucose monitoring device with multistage transdermal drug delivery module, Sci. Adv. 3 (2017), e1601314, https://doi.org/10.1126/sciadv.1601314.
[18] W. He, C. Wang, H. Wang, M. Jian, W. Lu, X. Liang, X. Zhang, F. Yang, Y. Zhang, Integrated textile sensor patch for real-time and multiplex sweat analysis, eaax0649, Sci. Adv. 5 (2019), https://doi.org/10.1126/sciadv.aax0649.
[19] A.J. Bandodkar, W. Jia, C. Yardımcı, X. Wang, J. Ramirez, J. Wang, Tattoo-based noninvasive glucose monitoring: a proof-of-concept study, Anal. Chem. 87 (2015) 394–398, https://doi.org/10.1021/ac504300n.
[20] J. Kim, J.R. Sempionatto, S. Imani, M.C. Hartel, A. Barfdokht, G. Tang, A. S. Campbell, P.P. Mercier, J. Wang, Simultaneous monitoring of sweat and interstitial fluid using a single wearable biosensor platform, Adv. Sci. 5 (2018), 1800880, https://doi.org/10.1002/advs.201800880.
[21] J. Kim, I. Jeerapan, S. Imani, T.N. Cho, A. Bandodkar, S. Cinti, P.P. Mercier, J. Wang, Noninvasive alcohol monitoring using a wearable tattoo-based iontophoretic-biosensing system, ACS Sens 1 (2016) 1011–1019, https://doi.org/10.1021/acssensors.6b00356.
[22] W. Gao, S. Emaminejad, H.Y.Y. Nyein, S. Challa, K. Chen, A. Peck, H.M. Fahad, H. Ota, H. Shiraki, D. Kiriya, D.-H. Lien, G.A. Brooks, R.W. Davis, A. Javey, Fully integrated wearable sensor arrays for multiplexed in situ perspiration analysis, Nature 529 (2016) 501–514, https://doi.org/10.1038/nature16521.
[23] A. Martín, J. Kim, J.F. Kurniawan, J.R. Sempionatto, J.R. Moreto, G. Tang, A. S. Campbell, A. Shin, M.Y. Lee, X. Liu, J. Wang, Epidermal microfluidic electrochemical detection system: enhanced sweat sampling and metabolite detection, ACS Sens 2 (2017) 1860–1868, https://doi.org/10.1021/acssensors.7b00729.
[24] G. Chen, J. Zheng, L. Liu, L. Xu, Application of microfluidics in wearable devices, small, Methods 3 (2019), 1900688, https://doi.org/10.1002/smtd.201900688.
[25] J.S. Nah, S.C. Barman, M.A. Zahed, M. Sharifuzzaman, H. Yoon, C. Park, S. Yoon, S. Zhang, J.Y. Park, A wearable microfluidics-integrated impedimetric immunosensor based on Ti3C2Tx MXene incorporated laser-burned graphene for noninvasive sweat cortisol detection, Sens. Actuators B: Chem. 329 (2021), 129206, https://doi.org/10.1016/j.snb.2020.129206.
[26] S. Li, Z. Ma, Z. Cao, L. Pan, Y. Shi, Advanced wearable microfluidic sensors for healthcare, Small 16 (2019), 1903822, https://doi.org/10.1002/smll.201903822.
[27] H. Lin, Y. Zhao, S. Lin, B. Wang, C. Yeung, X. Cheng, Z. Wang, T. Cai, W. Yu, K. King, J. Tan, K. Salahi, H. Hojaiji, S. Emaminejad, A rapid and low-cost fabrication and integration scheme to render 3D microfluidic architectures for wearable biofluid sampling, manipulation, and sensing, Lab Chip 19 (2019) 2844–2853, https://doi.org/10.1039/c9lc00418a.
[28] Y. Alvarez-Brana, J. Etxebarria-Elezgarai, L.R. de Larrinaga-Vicente, F.B. Lopez, L. Basabe-Desmonts, Modular micropumps fabricated by 3D printed technologies

for polymeric microfluidic device applications, Sens. Actuators B: Chem. 342 (2021), 129991, https://doi.org/10.1016/j.snb.2021.129991.
[29] F. Li, N.P. Macdonald, R.M. Guijt, M.C. Breadmore, Increasing the functionalities of 3D Printing microchemical devices by single material, multimaterial, and print-pause-print 3D-printing, Lab Chip 19 (2019) 35–49, https://doi.org/10.1039/c8lc00826d.
[30] N.P. Macdonald, J.M. Cabot, P. Smejkal, R.M. Guijt, B. Paull, M.C. Breadmore, Comparing microfluidic performance of three-dimensional (3D) printing platforms, Anal. Chem. 89 (2017) 3858–3866, https://doi.org/10.1021/acs.analchem.7b00136.
[31] V. Saggiomo, A.H. Velders, Simple 3D printed scaffold-removal method for the fabrication of intricate microfluidic devices, Adv. Sci. 2 (2015), 1500125, https://doi.org/10.1002/advs.201500125.
[32] S. Pandit, P. Singh, M. Sinha, R. Parthasarathi, Integrated QSAR and adverse outcome pathway analysis of chemicals released on 3d printing using acrylonitrile butadiene styrene, Chem. Res. Toxicol. 34 (2021) 355–364, https://doi.org/10.1021/acs.chemrestox.0c00274.
[33] A. Iuliano, E. van der Wal, C.W.B. Ruijmbeek, S.L.M. in 't Groen, W.W.M. Pim Pijnappel, J.C. de Greef, V. Saggiomo, Coupling 3D printing and novel replica molding for in house fabrication of skeletal muscle tissue engineering devices, Adv. Mater. Technol. 5 (2020), 2000344, https://doi.org/10.1002/admt.202000344.
[34] B. Stephens, P. Azimi, Z.E. Orch, T. Ramos, Ultrafifine particle emissions from desktop 3D printers, Atmos. Environ. 79 (2013) 334e339, https://doi.org/10.1016/j.atmosenv.2013.06.050.
[35] P. Azimi, D. Zhao, C. Pouzet, N.E. Crain, B. Stephens, Emissions of ultrafifine particles and volatile organic compounds from commercially available desktop three-dimensional printers with multiple filaments, Environ. Sci. Technol. 50 (2016) 1260–1268, https://doi.org/10.1021/acs.est.5b04983.
[36] T. Guo, T.R. Holzberg, C.G. Lim, F. Gao, A. Gargava, J.E. Trachtenberg, A.G. Mikos, J.P. Fisher, 3D printing PLGA: a quantitative examination of the effects of polymer composition and printing parameters on print resolution, Biofabrication 9 (2018), 024101, https://doi.org/10.1088/1758-5090/aa6370.
[37] J. Kim, S. McBride, B. Tellis, P. Alvarez-Urena, Y.-H. Song, D.D. Dean, V.L. Sylvia, H. Elgendy, J. Ong, J.O. Hollinger, Rapid-prototyped PLGA/β-TCP/hydroxyapatite nanocomposite scaffolds in a rabbit femoral defect model, Biofabrication 4 (2012), 025003, https://doi.org/10.1088/1758-5082/4/2/025003.
[38] A. Goyanes, A.B.M. Buanz, A.W. Basit, S. Gaisford, Fused-filament 3D printing (3DP) for fabrication of tablets, Int. J. Pharm. 476 (2014) 88–92, https://doi.org/10.1016/j.ijpharm.2014.09.044.
[39] C.G. Schirmeister, T. Hees, E.H. Licht, R. Mulhaupt, 3D printing of high density polyethylene by fused filament fabrication, Addit. Manuf. 28 (2019) 152–159, https://doi.org/10.1016/j.addma.2019.05.003.
[40] P. Azimi, D. Zhao, C. Pouzet, N.E. Crain, B. Stephens, Emissions of ultrafifine particles and volatile organic compounds from commercially available desktop three-dimensional printers with multiple filaments, Environ. Sci. Technol. 50 (2016) 1260–1268, https://doi.org/10.1021/acs.est.5b04983.
[41] Y. Kim, C. Yoon, S. Ham, J. Park, S. Kim, O. Kwon, P.-J. Tsai, Emissions of nanoparticles and gaseous material from 3d printer operation, Environ. Sci. Technol. 49 (2015) 12044–12053, https://doi.org/10.1021/acs.est.5b02805.
[42] J.S. Miller, K.R. Stevens, M.T. Yang, B.M. Baker, D.-H.T. Nguyen, D.M. Cohen, E. Toro1, A.A. Chen, P.A. Galie, X. Yu, R. Chaturvedi, S.N. Bhatia, C.S. Chen, Rapid casting of patterned vascular networks for perfusable engineered three-dimensional tissues, Nat. Mater. 11 (2012) 768–774, https://doi.org/10.1038/nmat3357.
[43] J. Lee, J. Paek, J. Kim, Sucrose-based fabrication of 3D-networked, cylindrical microfluidic channels for rapid prototyping of lab-on-a-chip and vaso-mimetic devices, Lab Chip 12 (2012) 2638–3642, https://doi.org/10.1039/c2lc40267j.
[44] Y. He, J. Qiu, J. Fu, J. Zhang, Y. Ren, A. Liu, Printing 3D microfluidic chips with a 3D sugar printer, Microfluid Nanofluidics 19 (2015) 447–456, https://doi.org/10.1007/s10404-015-1571-7.
[45] J. Qiu, Q. Gao, H. Zhao, J. Fu, Y. He, Rapid customization of 3D integrated microfluidic chips via modular structure-based design, ACS Biomater. Sci. Eng. 3 (2017) 2606–2616, https://doi.org/10.1021/acsbiomaterials.7b00401.
[46] A. Baraket, N. Zine, M. Lee, J. Bausells, N. Jaffrezic-Renault, F. Bessueille, N. Yaakoubi, A. Errachid, Development of a flexible microfluidic system based on a simple and reproducible sealing process between polymers and poly (dimethylsiloxane), Microelectron. Eng. 111 (2013) 332–338, https://doi.org/10.1016/j.mee.2013.02.059.
[47] S. Wang, S. Yu, M. Lu, L. Zuo, Microfabrication of plastic-PDMS microfluidic devices using polyimide release layer and selective adhesive bonding, J. Micromech. Microeng. 27 (2017), 055015, https://doi.org/10.1088/1361-6439/aa66ed.
[48] H.Y.Y. Nyein, L.-C. Tai, Q.P. Ngo, M. Chao, G.B. Zhang, W. Gao, M. Bariya, J. Bullock, H. Kim, H.M. Fahad, A. Javey, A wearable microfluidic sensing patch for dynamic sweat secretion analysis, ACS Sens 3 (2018) 944–952, https://doi.org/10.1021/acssensors.7b00961.
[49] D.K. Cai, A. Neyer, Polysiloxane based flexible electrical-optical-circuits-board, Microelectron. Eng. 87 (2010) 2268–2274, https://doi.org/10.1016/j.mee.2010.02.014.
[50] L. Tang, N.Y. Lee, A facile route for irreversible bonding of plastic-PDMS hybrid microdevices at room temperature, Lab Chip 10 (2010) 1274–1280, https://doi.org/10.1039/B924753J.
[51] Nae Yoon Lee Rajamanickam Sivakumar, Chemically robust succinimide group-assisted irreversible bonding of poly(dimethylsiloxane)–thermoplastic microfluidic devices at room temperature, Analyst 145 (2020) 6887–6894, https://doi.org/10.1039/D0AN01268H.
[52] J. Wu, N.Y. Lee, One-step surface modification for irreversible bonding of various plastics with a poly(dimethylsiloxane) elastomer at room temperature, Lab Chip 14 (2014) 1564–1571, https://doi.org/10.1039/c3lc51324f.
[53] H.N. Zhang, N.Y. Lee, Non-silicon substrate bonding mediated by poly (dimethylsiloxane) interfacial coating, Appl. Surf. Sci. 327 (2015) 233–240, https://doi.org/10.1016/j.apsusc.2014.10.172.
[54] W. Wu, J. Wu, J.H. Kima, N.Y. Lee, Instantaneous room temperature bonding of a wide range of non-silicon substrates with poly(dimethylsiloxane) (PDMS) elastomer mediated by a mercaptosilane, Lab Chip 15 (2015) 2819–2825, https://doi.org/10.1039/c5lc00285k.
[55] M.V. Hoang, H.-J. Chung and A.L. Elias, Irreversible bonding of polyimide and polydimethylsiloxane (PDMS) based on a thiol-epoxy click reaction, 26 (2016) 105019, ⟨http://doi.org/10.1088/0960–1317/26/10/105019⟩.
[56] A. Martín, J. Kim, J.F. Kurniawan, J.R. Sempionatto, J.R. Moreto, G. Tang, A. S. Campbell, A. Shin, M.Y. Lee, X. Liu, J. Wang, Epidermal microfluidic electrochemical detection system: enhanced sweat sampling and metabolite detection, ACS Sens. 2 (2017) 1860–1868, https://doi.org/10.1021/acssensors.7b00729.
[57] Y. Zhang, Y. Chen, J. Huang, Y. Liu, J. Peng, S. Chen, K. Song, X. Ouyang, H. Cheng, X. Wang, Skin-interfaced microfluidic devices with one-opening chambers and hydrophobic valves for sweat collection and analysis, Lab Chip 20 (2020) 2635–2645, https://doi.org/10.1039/d0lc00400f.
[58] R. Wang, Q. Zhai, Y. Zhao, T. An, S. Gong, Z. Guo, Q. Shi, b Z. Yong, W. Cheng, Stretchable gold fiber-based wearable electrochemical sensor toward pH monitoring, J. Mater. Chem. B. 8 (2020) 3655–3660, https://doi.org/10.1039/c9tb02477h.

Lei Wei received his Bachelor Degree in Mechanical and Electronic Engineering from Inner Mongolia University of Technology in 2011, and received his master's degree in Mechanical and Electronic Engineering from Chongqing University in 2014. He is currently pursuing a Ph.D. degree in the Faculty of Mechanical Engineering & Automation at Zhejiang Sci-Tech University. His research interests include flexible electronics and microfluidic devices.

Guoqing Fang received his Bachelor Degree in Biomedical Engineering from Nantong University in 2019. He is currently pursuing a master's degree in College of Science at Zhejiang Sci-Tech University. His research interest is developing novel functional materials for wearable physical/chemical sensors.

Zhongwen Kuang received his Bachelor Degree in Material Forming and Control Engineering from Jing-gang-shan University in 2019. He is currently pursuing a master's degree in College of Science at Zhejiang Sci-Tech University. His research interest is developing novel materials for intelligent actuators.

Lin Cheng received her Bachelor of Henan University in 2017. She is currently pursuing a Ph.D. degree in the Zhejiang Sci-Tech University. Her research interests include flexible sensor and smart materials/structures.

Prof. Huaping Wu received his Ph. D degree in Engineering Mechanics from the Harbin Institute of Technology in 2009 and a Bachelor's degree from the Harbin Institute of Technology in 2002. He worked as a visiting scholar at the Kyoto University in 2014 and a postdoctoral research fellow at the City University of Hong Kong in 2012. He is currently a Professor in the School of Mechanical Engineering at Zhejiang University of Technology. His research mainly focuses on the mechanics of smart materials/structures, bionic machinery and bionic manufacturing, and flexible electronics devices.

Dr. Daoyou Guo received his Ph.D degree in Electronic Science and Technology from Beijing University of Posts and Telecommunications. He joined Zhejiang Sci-Tech University in 2016 and worked as a visiting scholar in Department of Electrical Engineering at Saga University in 2019. He is currently an Associate Professor in the Department of Physics at Zhejiang Sci-Tech University. His research mainly focuses on ultra-wide band gap semiconductor Ga_2O_3 materials and devices.

Prof. Aiping Liu received her Ph.D degree in Material Science from the Harbin Institute of Technology in 2008. She worked as a postdoctoral research fellow at the Nanyang Technological University from 2009 to 2011 and a visiting scholar at the University of Texas at Austin from 2019 to 2020. She is currently a Professor in the Department of Physics at Zhejiang Sci-Tech University. Her research mainly focuses on the functional inorganic/organic material, with special emphasis on developing novel materials including graphene with sensing and actuation characteristic for wearable physical/chemical sensors and intelligent actuators.